

# ULTRASOUND PROCESSING AND COMPUTING: REVIEW AND FUTURE DIRECTIONS

---

George York and Yongmin Kim

*Image Computing Systems Laboratory, Departments of Electrical Engineering and  
Bioengineering, University of Washington, Seattle, Washington 98195-7962; e-mail:  
ykim@u.washington.edu*

**Key Words** diagnostic ultrasound, color-flow imaging, three-dimensional  
ultrasound, programmable processing

■ **Abstract** Since the introduction of medical ultrasound in the 1950s, modern diagnostic ultrasound has progressed to see many major diagnostic tools come into widespread clinical use, such as B-mode imaging, color-flow imaging, and spectral Doppler. New applications, such as panoramic imaging, three-dimensional imaging, and quantitative imaging, are now beginning to be offered on some commercial ultrasound machines and are expected to grow in popularity. In this review, we focus on the various algorithms, their processing requirements, and the challenges of these ultrasound modes. Whereas the older, mature B and color-flow modes could be systematically implemented using hardwired components and boards, new applications, such as three-dimensional imaging and image feature extraction, are being implemented more by using programmable processors. This trend toward programmable ultrasound machines will continue, because the programmable approach offers the advantages of quick implementation of new applications without any additional hardware and the flexibility to adapt to the changing requirements of these dynamic new applications.

## CONTENTS

Introduction .....	560
Diagnostic Ultrasound Imaging .....	560
Echo Imaging (B-Mode) .....	562
<i>Temporal, Spatial, and Frequency Compounding</i> .....	563
<i>Other Filters</i> .....	563
Spectral Doppler .....	563
Color-Flow Imaging .....	564
<i>Clutter Filtering (Wall Filter)</i> .....	564

The US Government has the right to retain a nonexclusive, royalty-free license in and to any copyright covering this paper.

<i>Color-Flow Velocity Estimate</i> .....	565
<i>Color-Flow Trade-offs and Challenges</i> .....	567
Image Processing and Display .....	571
<i>Segmentation and Quantitative Measurements</i> .....	573
<i>Panoramic Imaging</i> .....	575
Three-Dimensional Ultrasound .....	575
<i>Acquisition</i> .....	577
<i>Reconstruction Techniques</i> .....	578
<i>Visualization</i> .....	579
<i>Computational Requirements</i> .....	580
<i>Clinical Applications of 3D</i> .....	581
Processing Challenge .....	582
Conclusions .....	583

## INTRODUCTION

Diagnostic ultrasound has become the most common medical-imaging modality, and it is far from stagnant as the number of clinical applications for ultrasound continues to grow. Ultrasound is routinely used in all clinical medicine specialties and in many areas of bioscience research. It is a popular modality because it is safe, noninvasive, portable, easy to use, relatively inexpensive, and displays images in real time (104). Even as a mature technology, advances are still being made, ranging from improvements in transducer design to new signal processing algorithms, including the introduction of new modes and applications, such as three-dimensional (3D) imaging.

In this review, we focus on the current status of ultrasound imaging and the impact of new applications on the design of current and future ultrasound machines. We discuss the various algorithms, processing requirements, and challenges of the common diagnostic ultrasound modes, including B-mode and color-flow imaging. We also discuss the processing challenges of several new advanced applications, such as panoramic imaging, 3D imaging, and automatic quantitative measurements.

## DIAGNOSTIC ULTRASOUND IMAGING

Figure 1 schematically illustrates the processing stages of a typical diagnostic ultrasound system. The ultrasound acoustic signals are generated by converting pulses of a 2- to 10-MHz electrical signal (known as the carrier frequency  $\omega_c$ ) from the transmitter into an acoustic wave using a piezoelectric transducer. As the acoustic wave pulse travels through the tissue, a portion of the pulse is reflected at the interface of materials with different acoustical impedance, creating a returned signal that highlights features, such as tissue boundaries along a fairly

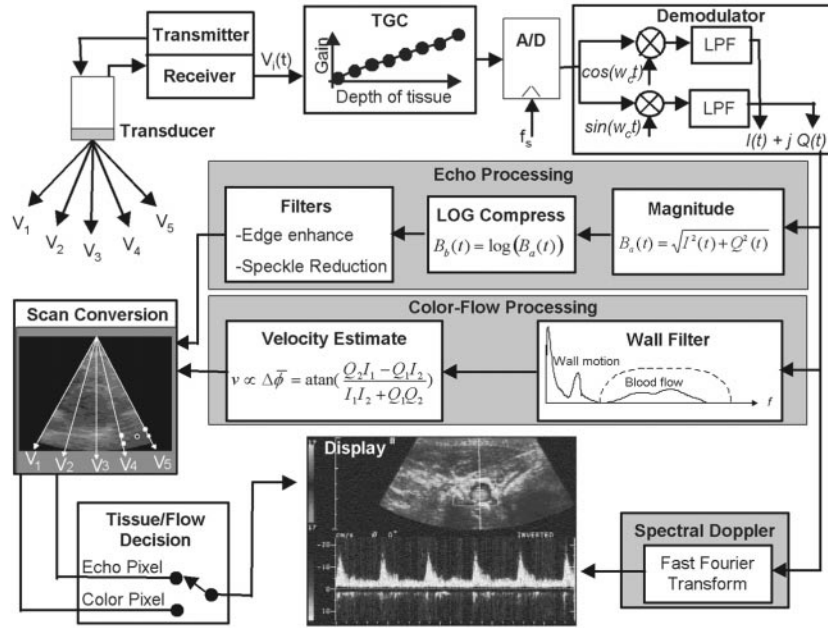


FIGURE 1 Block diagram of a typical diagnostic ultrasound machine.

well defined beam line. The reflected pulses are sensed by the transducer, and converted into radio frequency (RF) electrical signals. The transducer emits the acoustic pulses at a pulse repetition frequency (PRF) typically ranging from 0.5 to 20 kHz, based on the time for the pulse to travel to the maximum target depth and return to the transducer.

As the acoustic wave travels through the tissue, its amplitude is attenuated. Therefore, the receiver first amplifies the returned signal in proportion to depth or the time required for the signal to return (i.e. time-gain compensation, TGC). The signal's attenuation also increases as  $\omega_c$  is increased, limiting the typical ultrasound system to depths of 10–30 cm. Higher frequencies, such as 50 MHz, are limited to a <1-cm depth, but they offer the advantage of improved resolution, which could be useful for applications in eye, skin, and intravascular imaging (57).

After the RF analog signal is received and conditioned through time-gain compensation, it is typically sampled at a conservatively high rate (e.g. 36 MHz for a transducer with  $\omega_c = 7.5$  MHz). The demodulator then removes the carrier frequency by using techniques such as quadrature demodulation to recover the return (echo) signal. In quadrature demodulation the received signal is multiplied with  $\cos(\omega_c t)$  and  $\sin(\omega_c t)$ , which after low-pass filtering, results in the baseband signal of complex samples,  $I(t) + jQ(t)$ . The complex samples contain both the

magnitude and phase information of the signal and are needed to detect moving objects, such as blood flow.

The samples of the signal obtained from one acoustic pulse (i.e. one beam) are called a vector. Today's phased-array transducers can change the focal point of the beam as well as steer the beam by changing the timing of the firing of the piezoelectric elements that comprise the array. By steering these beams and obtaining multiple vectors in different directions along a plane (i.e.  $V_1$ – $V_5$  in Figure 1), a two-dimensional (2D) image can be formed. Depending on how the vectors are processed, the image can be simply a gray-scale image of the tissue boundaries (known as echo imaging or B-mode) or also have a pseudocolor image overlaid, where the color represents the speed and direction of blood flow (known as color-mode) as shown in Figure 2 (see color figure). In addition, the spectrum of the blood velocity at a single location over time can be tracked (known as gated Doppler spectral estimation) and plotted in a spectrogram as shown in the bottom of Figure 2. By combining multiple slices of these 2D images, 3D imaging is also possible for these modes. Depending on the application, typical frame rates can range from 5 to 30 frames per second (fps) for 2D color-flow imaging to >50 fps for 2D B-mode imaging (8).

## ECHO IMAGING (B-MODE)

Real-time B-mode scanning has been in use for the last 2 decades and is still the most frequently used ultrasound mode by clinicians, allowing them to image in real time the various tissue structures throughout the body. The B-mode image is created by first taking the magnitude (envelope detection) of the quadrature signal,  $B_a(t) = \sqrt{I^2(t) + Q^2(t)}$ . Then the signal is logarithmically compressed,  $B_b(t) = A \log[B_a(t)] + C$ , to reduce the dynamic range from the sampled range (around 12 bits) to that of the output display (8 bits) and to nonlinearly map the dynamic range to enhance the darker-gray levels at the expense of the brighter-gray levels (32).

Several techniques are used to improve the quality of the image. Edge-enhancing filters are used to sharpen the tissue boundaries. These filters also enhance the noise in the image, which is typically dominated by speckle. Due to the transmitted acoustic pulse having a finite size as it travels through the body, different scatterers that are closely spaced may reflect parts of the same beam. When these reflected parts arrive back to the transducer, they may be in phase or out of phase. The combined reflected acoustic energy will show both constructive and destructive interference, resulting in a granular pattern called speckle. Even though B-mode imaging is very mature, suppressing speckle noise without degrading the image signal is still a challenge. This is further complicated by the fact that some speckle patterns are used by clinicians to distinguish different tissue regions, such as fat versus muscle (51). The following discusses various speckle-filtering techniques, which usually can be turned on or off as needed by the clinician.

## Temporal, Spatial, and Frequency Compounding

Compounding averages multiple images of the same target obtained under different imaging conditions designed to have uncorrelated speckle patterns. This averaging enhances the stationary signal (i.e. tissue boundaries) while reducing the varying speckle noise. Temporal compounding assumes that the frame rate is low enough to ensure the speckle is uncorrelated, and averages the current unfiltered image  $B_{in}$  with the previous output image  $B_{out}$ , i.e.,  $B_{out}(k) = a \cdot B_{out}(k-1) + (1-a) B_{in}(k)$ , where  $k$  is the frame number and  $a$  is the weight (or persistence) (34). This can cause streaking of fast-moving objects (46). To avoid this,  $a$  can be made to adapt to quick changes, i.e. let  $a = f[1/|B_{in}(k) - B_{out}(k-1)|]$ .

In spatial compounding, the uncorrelated speckle patterns are generated by varying the spatial orientation (i.e. illumination angle) of the aperture relative to the target (101), while in frequency compounding, the acoustic frequency is varied to create the uncorrelated speckle patterns (60). Spatial compounding is more complicated as the images must be spatially registered with respect to each other before they are interpolated. Both of these techniques require multiple images to be acquired to produce an averaged output frame, which decreases the frame rate.

## Other Filters

Linear filters tend to introduce severe blurring and loss of diagnostically significant information (58); thus, several nonlinear filters have been attempted, such as simple three-tap median filters (73) that are known for preserving edges while reducing the noise. However, the statistical characteristics of the speckle throughout ultrasound images are not consistent, with some regions behaving as fully formed speckle (i.e. high density of random scatterers with small spacing compared to wavelength of ultrasound), which can be modeled as a Rayleigh distribution and filtered accordingly, and other regions behaving as partially formed speckle, requiring higher-order statistics to model (i.e. Rician and homodyned-K distributions) (32). Adaptive techniques have been developed to adjust the amount of filtering pixel by pixel based on the speckle texture in a local window. For example, Loupas et al (58) used an adaptive algorithm that measures the local homogeneity (i.e. weighted median) in a  $9 \times 9$  window and adapted the smoothing for each pixel, whereas Bamber (2) used an unsharp masking filter, in which the amount of smoothing is controlled by the local mean and variance in a  $7 \times 7$  window. These nonlinear filters require a large amount of computation and present a challenge to implement in real time.

## SPECTRAL DOPPLER

Although B-mode imaging is useful for observing the spatial relationship between tissue layers in the body and for monitoring moving structures, such as the heart and fetus, it cannot be used for visualizing faster motion, such as blood flow. The

ability to assess the velocity of moving blood cells in the body is important for many clinical situations, such as detecting the degree of stenosis in a vessel, monitoring the cardiac cycle, and assessing the blood flow to the fetus. In continuous-wave ultrasound systems, the velocity can be estimated from the Doppler shift of the continuously transmitted signal. In pulsed ultrasound systems, the velocity of a sample volume is estimated from

$$v \cong \frac{c \cdot PRF}{2\omega_c \cos\theta} \Delta\phi = \frac{c}{2\omega_c \cos\theta} f_d, \quad (1)$$

where  $c$  is the velocity of sound in blood,  $\theta$  is the Doppler angle,  $\Delta\phi$  is the phase difference between two consecutive pulses, and  $f_d$  is the Doppler shift. When observing multiple signals received from a single sample volume containing multiple moving scatterers, a spectrum of frequencies can be detected, corresponding to the flow in the sample volume. Therefore, gated Doppler spectral estimation tracks the Doppler frequencies at a single spatial location over time by collecting a large number of ensembles (e.g. 256 samples) at one location, then it performs a one-dimensional fast Fourier transform (FFT). Plotting the spectrum of velocities vertically versus time horizontally creates a spectrogram, as shown in Figure 2.

## COLOR-FLOW IMAGING

Spectral Doppler can accurately quantify the blood flow at a specific location. In order to visualize the distribution of flow, the velocity of the blood flow for a specified region is mapped to a pseudocolor image and overlaid on top of a 2D B-mode image in real time (i.e. 10 fps), as shown in Figure 2. The magnitude and direction of the velocity toward and away from the transducer (i.e. axial direction) are displayed as the brightness of colors, typically red and blue, respectively. This is known as color-flow imaging. Its main processing steps are wall filtering and velocity estimation.

### Clutter Filtering (Wall Filter)

In addition to the desired signal from the blood scatterers, the received signal contains clutter noise returned from the surrounding tissue and slowly moving vessel walls. The frequency components due to wall motion are low, e.g. <1 kHz, while the blood motion frequency is typically around 15 kHz (37). Due to the smooth structures of the walls, the clutter signal can be much stronger (i.e. about 40 dB) than the scattered signal from the blood (90). Many high-pass filters have been developed to remove the unwanted clutter signal. These techniques include stationary echo canceling, finite impulse response (FIR), infinite impulse response (IIR), and regression filters (42). Of these techniques, regression filters have been shown to have better performance compared to other techniques (45). These filters

are designed to filter the clutter adaptively by first estimating the clutter frequency and then using this estimated frequency to filter clutter effectively.

Regression wall filters treat their inputs as polynomial functions in the time domain and operate on the assumption that the slowly varying clutter component in the Doppler signal can be approximated by a polynomial of a given order (41). Once approximated, this component can then be subtracted from the original signal so that the contribution from the blood flow can be retrieved and analyzed. Mathematically, it can be described by

$$y(k) = x(k) - \sum_{d=0}^D a_d k^d \quad k = 1, 2, \dots, E, \quad (2)$$

where  $x(k)$  and  $y(k)$  are input and output signals at ensemble  $k$ ,  $a_d$  are the regression model coefficients, and  $D$  is the regression order. Accurately determining  $a_d$  requires a computationally intense Vandermonde matrix multiplication (45). Basoglu (4b) developed a wavelet-based method, which reduced these computations by 22% with an accuracy similar to normal regression and better than the FIR and IIR techniques.

## Color-Flow Velocity Estimate

The velocity estimate for color flow could be done using the FFT. However, to obtain an accurate velocity resolution (e.g. 128 levels) would require taking an equal number of ensembles per scan line, which would considerably slow down the frame rate. Computing the FFT with only few ensembles leads to an unreliable velocity estimate. Therefore, other velocity estimation techniques are used in diagnostic ultrasound and can be divided into two main categories: phase-shift and time-shift techniques. In the phase-shift technique, the velocity is estimated based on the phase shift from signals at a fixed depth while in the time-shift technique, a moving window is used to track blood movement over a changing depth to estimate the velocity.

**Phase-Shift Velocity Estimate** The most common method to detect the velocity is to measure the change in phase  $\Delta\phi$  (equation 1) by acquiring multiple vectors (i.e.  $V_e$ ,  $V_{e+1}$ , and  $V_{e+2}$  in Figure 3) along a single scan line with the transducer stationary, and then calculate the average change in phase at each range bin along the scan line (47). Barber et al (3) showed that computing the first lag of auto-correlation is sufficient to correctly estimate the change in phase  $\Delta\phi$  for each range bin  $t$ :

$$\Delta\phi(t) = \arctan\left(\frac{\sum_{e=0}^{E-2}[Q_e(t)I_{e+1}(t) - I_e(t)Q_{e+1}(t)]}{\sum_{e=0}^{E-2}[I_e(t)I_{e+1}(t) + Q_e(t)Q_{e+1}(t)]}\right), \quad (3)$$

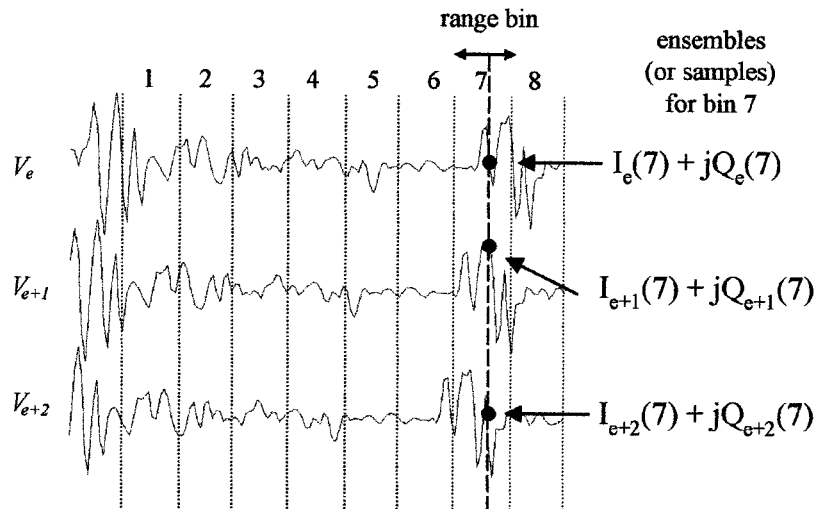


FIGURE 3 Example of autocorrelation velocity estimate.

where the denominator and numerator are respectively the real and imaginary part of the first lag of autocorrelation, and  $E$  is the ensemble size, varying from 4 to 16. In Figure 3, the waveforms of the three vectors appear to be moving to the left (toward the transducer) over time. Three ensemble samples after demodulation, i.e.  $I(t) + jQ(t)$ , for the 7<sup>th</sup> range bin are used to illustrate the data needed to estimate  $\Delta\phi$  for this range bin.

**Time-Shift Velocity Estimate** The time-shift estimation technique requires tracking the movement of a group of blood cells by using the intensity of their echoes. The predominantly used time-shift estimation method is the cross-correlation technique (13). Velocity is estimated by a one-dimensional correlation between the RF echo vectors (i.e.  $V_e$ ,  $V_{e+1}$ , and  $V_{e+2}$  in Figure 4) collected from consecutively transmitted ultrasonic pulses along the same beam line. The vectors are divided into several range bins as shown in Figure 4. The cross-correlation is calculated first:

$$R(\tau, i) = \frac{1}{N(E-1)} \sum_{e=1}^{E-1} \sum_{n=0}^{N-1} V_e(n + iN) \cdot V_{e+1}(n + iN + \tau), \quad (4)$$

where  $\tau$  is the number of lags,  $i$  denotes the bin number, and  $N$  is the number of samples in a bin. The velocity at the corresponding bin is

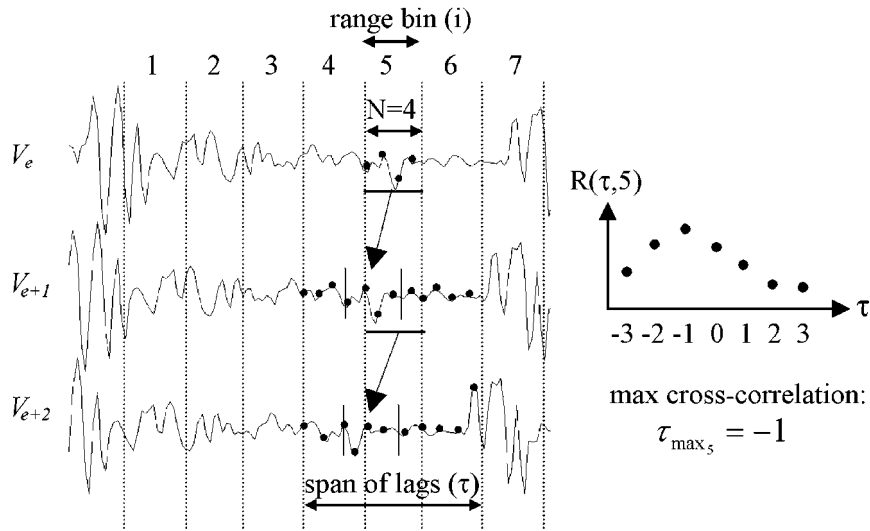


FIGURE 4 Example of cross-correlation velocity estimate.

$$v = \frac{c}{2} \frac{\tau_{\max_i}}{f_s} \cdot PRF, \tag{5}$$

where  $\tau_{\max_i}$  is the lag at which the maximum correlation occurred for the  $i^{th}$  range bin and  $f_s$  is the RF sampling frequency, which is fourfold or more the center frequency of the transducer for proper sampling (42). Often these quantized velocity estimates have too coarse a resolution to give a smooth-looking image. A parabola can be fit to the cross-correlation values for the different lags of a range bin.  $\tau_{\max_i}$  can be determined by locating the parabola peak. Using this interpolated lag to estimate the velocity decreases the apparent quantization and improves the image appearance (13).

### Color-Flow Trade-offs and Challenges

Both the phase-shift and time-shift velocity estimation techniques present various trade-offs and challenging problems.

**Aliasing** The speed of blood is typically a few centimeters per second, but it can increase to as high as 10 m/s in a stenotic area. In addition, the cardiac cycle creates a pulse wave propagating along the blood flow in the arteries that can also travel at speeds as high as 10 m/s (9). For the phase-shift technique, the maximum velocity that can be measured without aliasing depends on the PRF and center frequency of the transducer:

$$v_{\max} = \frac{c}{4} \frac{PRF}{f_c} \quad (6)$$

While the clinician can increase the PRF (thus, the maximum measurable velocity) by decreasing the imaging depth, aliasing can still occur in the color-flow image. An example of aliasing can be seen in Figure 2 in the carotid artery, which is predominantly blue-green, then transitions from white to yellow to red. This red is not reversed blood flow, but instead faster blood flow in the same direction as the blue-green, but it has aliased over the pseudo-color range.

Various improvements have been investigated to reduce the aliasing problem. One method is to use the cross-correlation time-shift technique, in which the maximum velocity theoretically has no limit as long as the number of lags can be increased, as indicated in equation 5. However, the width of the blood vessel cross section, computing capability, or both eventually limits the number of lags and the maximum velocity measured. In another approach, Nitzpon et al (72) used dual transmit frequencies ( $f_a$  and  $f_b$ ), increasing the maximum velocity by  $f_a/(f_b - f_a)$ , thus reducing the aliasing. For the spectral Doppler FFT techniques, temporal tracking methods have been investigated to detect when the velocity estimates cross the aliasing boundary, then correct the velocity estimates accordingly (100). For color-flow imaging, the velocity changes between two successive frames can be large, making temporal tracking impractical. Instead, spatial tracking along a scan line (i.e. across a vessel's velocity profile) has been shown to perform well for laminar flow (91).

**Resolution** The transmitted signal is not a single frequency, but a spectrum of frequencies. The attenuation of the ultrasound signal as it travels through the tissue is frequency-dependent, with larger attenuation for the higher frequency components. As a result, the center frequency of the received signal is shifted down compared to the originally transmitted  $f_c$  (42). This frequency shift is more pronounced for broadband signals, resulting in increasing the variance of the velocity estimate. Thus, narrowband signals are used to reduce the variance of the velocity estimate when using the phase-shift technique. This is at the expense of axial resolution, because broadband signals have better axial resolution. The axial resolution ( $AR$ ) of the transducer is approximated by

$$AR = \frac{Q}{4} \frac{c}{f_c}, \quad (7)$$

where  $Q$  is the quality factor or the number of oscillations in the pulse (19). A narrowband signal (i.e.  $Q = 8$  to  $15$ ) is normally used for color-flow imaging using the phase-shift autocorrelation technique (42), resulting in an axial resolution of 0.4 to 0.8 mm for a 7.5-MHz transducer. On the other hand, a broadband signal (i.e.  $Q = 2$  to  $5$ ) can be used for color-flow imaging using the time-shift technique and has a better axial resolution of 0.1 to 0.25 mm for a 7.5-MHz transducer. However, because of a low SNR associated with broadband signals

(13), it is possible that multiple peaks in the cross-correlation can occur leading to selecting the incorrect lag, thus an inaccurate velocity estimate.

**Computation Requirement** Comparisons of the phase-shift and time-shift techniques for blood flow imaging conclude that the time-shift estimation technique is generally more accurate (40). However, most commercially available systems use the phase-shift technique (49). This is partly due to overcoming the inertia and development cost of switching to a new technique and partly due to the large amount of computation required by the time-shift estimation technique, which must process at the higher RF sampling rate, whereas the phase-shift techniques process at the baseband data rate. We estimate the demodulation and velocity estimation subsystems require about 32 billion operations per second (BOPS) for the time-shift technique using cross-correlation and about 7 BOPS for the phase-shift technique using autocorrelation.

To reduce large computation required by the full cross-correlation, other time-shift techniques have been researched. Bonnefous et al (13b) simplified the computation of full cross-correlation with a system based on one-bit cross-correlation, resulting in a slight deviation compared with the true velocity. DeJong et al (27) developed a correlation-interpolation method, which correlates based only on five selected lags, but still incurs the computation cost of transcendental functions (i.e. arctan, arccos, arcsin) to implement the interpolation. Other methods include the maximum likelihood estimator (36) and butterfly search technique (1), which use a model to predict the most likely trajectory of the blood between pulses, reducing the complete search required by cross-correlation. In addition, the 2D sum of absolute difference (SAD) approach demonstrated by Bohs et al (11) searches for the minimum SAD

$$SAD_{x,y} = \sum_i \sum_j \left| X_{i,j}(k) - X_{i+x,j+y}(k-1) \right| \quad (8)$$

between successive frames over a given kernel size. This search is similar to full cross-correlation, but the SAD computation is less expensive than cross-correlation.

**Limited Frame Rate** Although B-mode imaging can achieve real-time frame rates (e.g. >30 fps), color-flow imaging is often pseudo-real time, limited by the following formula:

$$\text{flow frame rate} = \frac{PRF \cdot \text{beams}}{E \cdot C_{\text{vectors}} + K \cdot B_{\text{vectors}}}, \quad (9)$$

where  $K$  is the relative ratio between the B-mode frame rate and color-flow frame rate,  $C_{\text{vectors}}$  and  $B_{\text{vectors}}$  are the number of color-flow image vectors and B-mode image vectors, respectively, and  $\text{beams}$  is the number of beams fired in parallel. The  $PRF$  is limited by the imaging depth and the speed of sound in medium (i.e.

1540 m/s). Because the speed of sound cannot be modified, decreasing the depth is the only way to increase the *PRF*. Increasing the number of beams fired simultaneously (or interleaved) (106) can increase the frame rate. However, the side lobes and grating lobes of the parallel beams can interfere with each other, thus increasing the noise and artifacts in the image. Another possibility for increasing the frame rate is to decrease the number of ensembles at a cost of decreasing the accuracy of the velocity estimate. Finally, decreasing the number of vectors can increase the frame rate, but this is at the expense of either decreasing the spatial resolution over the ROI or maintaining the spatial resolution but decreasing the size of the ROI.

The clinician must consider the above trade-offs of frame rate versus accuracy, resolution, and noise. A slow color-flow frame rate can miss details of higher-frequency events, such as in the cardiac cycle. Because the color-flow frame rate can be much less than the B-mode image rate, this results in different temporal and spatial relationships between the two modes in the output image sequence, e.g. the B-mode image could be in diastole while the color-flow image is in systole.

**Velocity Dependence on Doppler Angle** The current velocity estimation techniques can only sense the axial component of the velocity, while the true velocity can be in any direction with a different magnitude than the color displayed. The positioning of the transducer and interpretation of the color-flow images rely highly on the skill of the clinician. Confusion can occur for sinuous blood vessels that change direction relative to the axis of the transducer beam throughout the image. The change in vessel direction causes a color change in the image even if there is no true velocity change. Likewise, if a sector scan is made with a curvilinear transducer, the axial components of the beams are not parallel and diverge from the transducer head. Thus, the clinician must keep in mind that the Doppler angle is not constant, but it changes across the image. In addition, it is often assumed that the blood flows through a vessel parallel to the vessel axis. However, flow in certain arteries, such as the aorta arch, is helical (i.e., like water exiting the bathtub drain) (9). Thus, the true direction of helical flow across an artery cross-section can be constantly changing relative to the transducer beam axis, varying the output color map even though the true velocity magnitude may be constant. One method to alleviate this confusion is to use power-mode imaging, in which only the power of the blood flow is displayed rather than the speed and direction. Power mode has higher sensitivity (i.e. SNR), less aliasing artifacts, and decreased dependence on Doppler angle than color-flow, thus has an advantage in reliably detecting blood flow, particularly in smaller vessels and in segmenting the vessels for 3D imaging (90).

To sense the flow in more dimensions than axial, other methods have been developed. Overbeck et al (77) developed a vector Doppler system that attempts to measure the true velocity vector, including the magnitude and direction using multiple transducers in a fixed geometry. Other methods have been developed to

sense the transverse flow in addition to the axial flow. Bohs et al (11) developed a 2D time-shift method, which searches for the minimum SAD (equation 8) between successive frames over a given kernel size. The  $x, y$  coordinates for the minimum SAD determine the 2D velocity vector. Similarly, 2D cross-correlation could be performed, but it would require more computation (85).

### IMAGE PROCESSING AND DISPLAY

After the B-mode and color-flow data are acquired and processed, the polar coordinate data must then be spatially transformed to the geometry and scale of the sector scan on the Cartesian raster output image through a process known as scan conversion (75). As Figure 5 shows, when a sector scan is made using a curvilinear transducer, each Cartesian raster pixel value  $P(x,y)$  must be interpolated from its surrounding polar vector data  $V_{\psi}(r)$ . Parker & Troxel (79) compared the effect of various interpolation methods (i.e. nearest neighbor, bilinear, windowed sinc, cubic splines), and Berkhoff et al (10) compared the speed of these algorithms on a general purpose computer. The key tasks for scan conversion are (a) to calculate the address of the input data (i.e. a polar conversion, requiring  $\arctan(y/x)$  and  $\sqrt{x^2 + y^2}$ ) and the interpolation coefficient weights for each output pixel  $P(x, y)$ ; (b) to fetch the respective input data values and (c) compute the interpolation. York et al (107) demonstrated that steps (b) and (c) can be done in

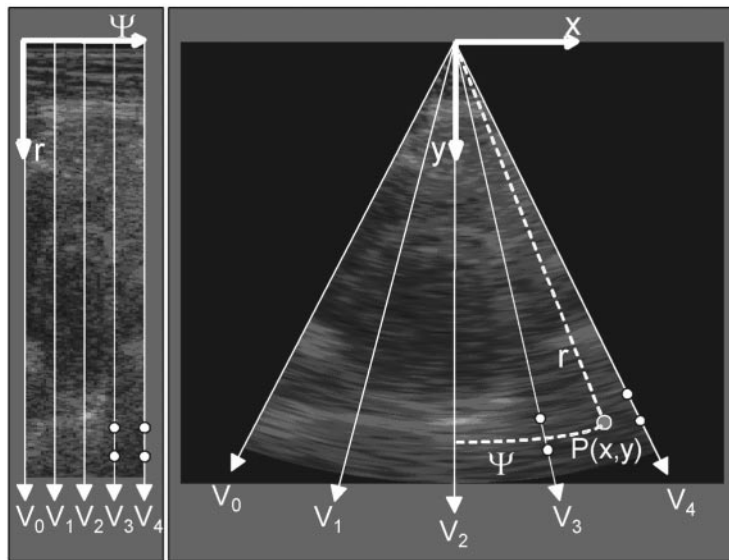


**FIGURE 5** (Left) Example data vectors before scan conversion and (right) after scan conversion.

real time on new advanced programmable DSPs (known as mediaprocessors) if the computations of step (a) are precomputed and stored in lookup tables. The main bottleneck is step (b) owing to the nonlinear relationship between the input and output pixels. For example, to calculate one row with five output pixels shown in Figure 6(a), the sets of input data needed are stored nonsequentially along an arc in memory as shown in Figure 6(b). Today's SDRAM memory and cache-based architectures are optimized for sequential memory access, not the random access as needed in Figure 6(b); thus input/output limits the speed of scan conversion.

Following scan conversion, if the B-mode and color-flow images are obtained at different frame rates, then either frame interpolation or temporal compounding can be used to increase the apparent frame rate of the slower image. Then, tissue/flow decision determines whether a gray-scale tissue pixel or color-flow pixel should be output for each pixel in the ROI. The decision is based on predetermined thresholds for parameters, such as the echo gray-level value, the magnitude and phase of the velocity vector, and the variance and power of the velocity (49). This is typically the last stage for current ultrasound machines. In future machines, this stage could also perform more advanced image processing, such as auto-

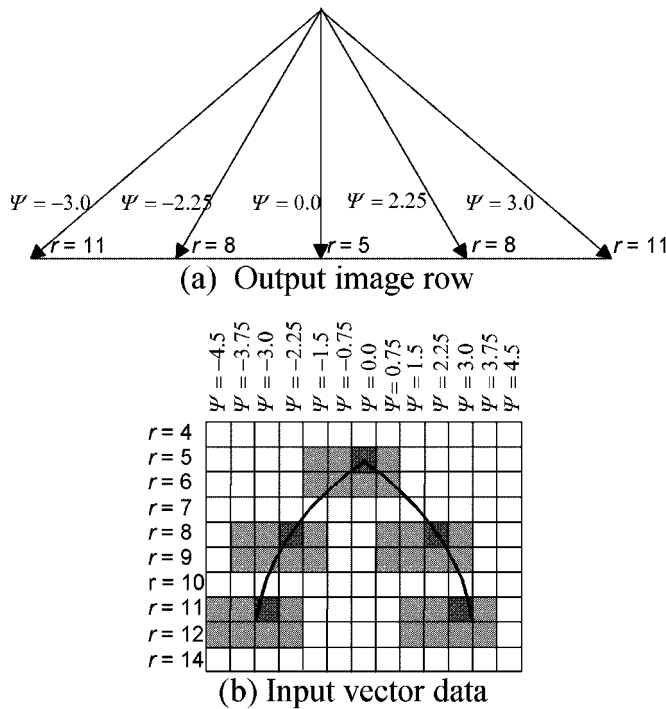
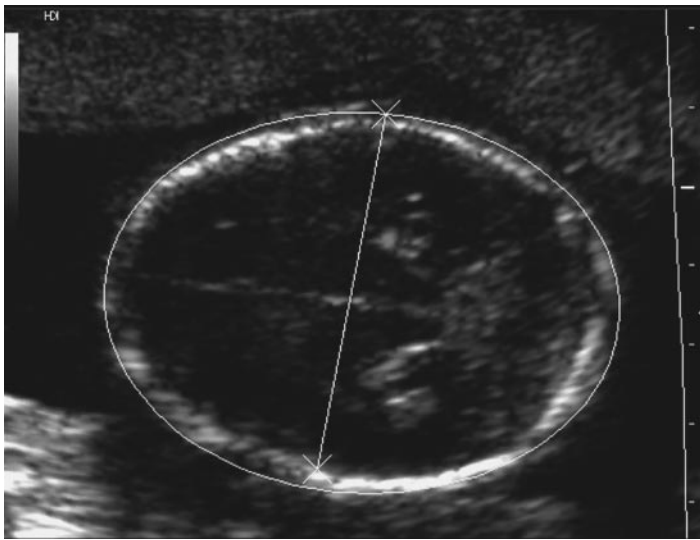


FIGURE 6 Nonsequential data access required by scan conversion.

matically segmenting images and creating different views of several obtained images, e.g. panoramic imaging and 3D imaging.

## Segmentation and Quantitative Measurements

Many researchers have investigated various image processing algorithms for automatic segmentation, classification, and measurements of various features of clinical interest. For example, Pathak et al (80) created a semi-automatic fetal head measurement application based on active contour models (snakes) as shown in Figure 7. The clinician must select a point inside the head, and then the algorithm automatically finds the contour and measures diagnostically important parameters, such as biparietal diameter (BPD) and head circumference (HC). Active contour models have also been applied to automatically segment the boundaries in ultrasound images for the fetal abdomen (17), the cortex of the brain (26), ovarian follicles (68), and for left-ventricular boundaries in echocardiograms, allowing measurements of ejection fraction and regional wall thickening (16, 30). Automatic segmentation and detection has also been done for the fetal femur by using mathematical morphology algorithms (97) and for prostate contours for volume estimation by using a matched filter to find the centroid followed by an edge-linking algorithm (18). Pathak et al (81) developed a linear feature enhancement technique to detect the pubic arch automatically via transrectal ultrasound for the accurate assessment of pubic arch interference (see Figure 8) in prostate brachytherapy (i.e. a surgical procedure for treating localized prostate cancer by implanting radioactive seeds), replacing the need of current CT-based techniques.



**FIGURE 7** Automatic fetal head measurement using active contour models (snakes).

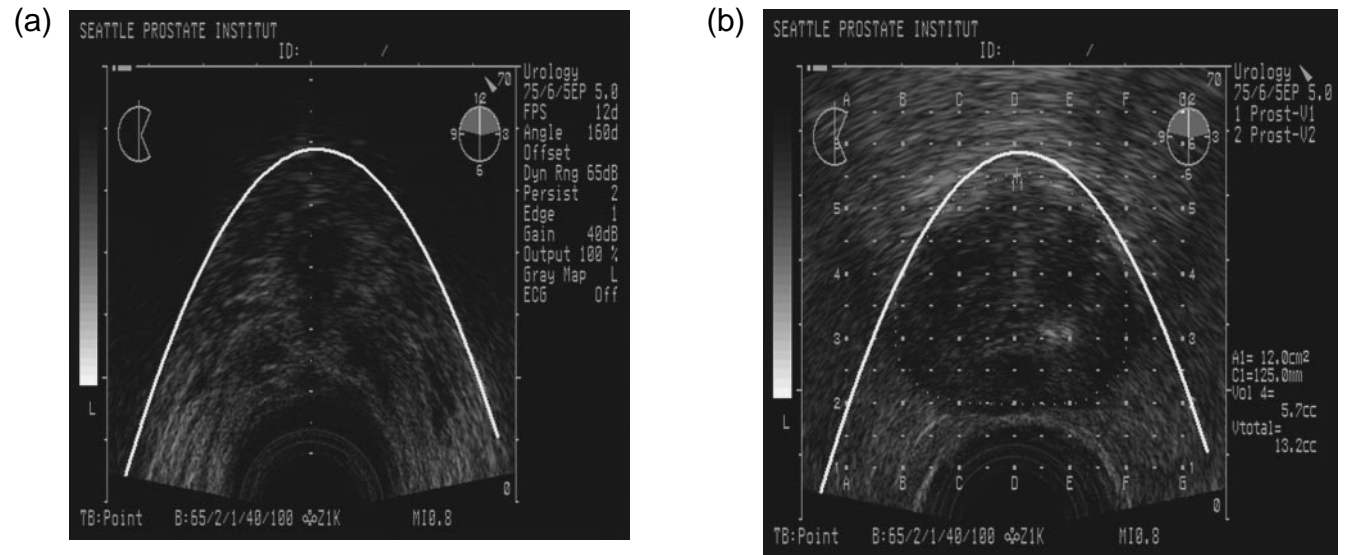


**FIGURE 8** (a) Image cross-section containing the automatically detected pubic arch. (b) The detected arch superimposed on the neighboring (transverse) cross-sectional prostate image used to determine if the pubic arch interferes with the prostate during the planning stage of brachytherapy.

Ultrasound images generally have low signal-to-noise ratios, making segmentation challenging and making it difficult to define a “gold standard” for comparison purposes. Manual segmentation by multiple experts can result in a large variation in measurements, called interobserver variability, whereas reliable (semi-)automatic segmentation methods offer the potential advantage of making the measurement process more consistent (80). However, proper evaluation of these segmentation algorithms is essential and should involve rigorous statistical methods to quantitatively assess the performance and determine if an automatic algorithm agrees with the multiple experts’ segmentation as much as the different experts agree with each other (15b).

## Panoramic Imaging

The 2D B-mode and color-flow images have a limited field of view, allowing the visualization of only portions of larger organs [e.g. the renal transplant in Figure 9(a)] to be seen at a time. To extend the field of view to see larger organs and their surroundings [e.g. the renal transplant, liver, and distal fluid collection in Figure 9(b)], Weng et al (105) developed a technique whereby, as the clinician slides the transducer across the area of interest, new images are acquired, registered, warped, and interpolated into a panoramic image in real time without the use of a position sensor.

To support these demanding processing requirements, a board with two programmable mediaprocessors (Texas Instruments TMS320C80) is integrated inside an otherwise hardwired ultrasound machine (48), with one mediaprocessor handling the registration and the other handling the translation, rotation, and blending. This extended field-of-view technique has been upgraded to support color-flow and power-mode imaging and can be used to measure larger structures in the panoramic image. Kroger et al (52) evaluated panoramic imaging’s ability to measure anatomic dimensions of structures, such as human legs, and found that it underestimates linear distances by 1.7% ( $\pm 2.2\%$ ), which is similar to the spatial error range of normal B-mode imaging.

## THREE-DIMENSIONAL ULTRASOUND

Although many researchers have studied 3D ultrasound for >20 years, only recently, owing to advances in computing power, has it been seriously considered for routine clinical use. Some clinical benefits that have been identified include the ability to obtain views not possible with 2D imaging (35, 69), the increased understanding of complex geometric structures (69), the ability to image more reproducibly (35), and the ability to accurately measure distances and volumes (24, 78, 86). Despite these potential benefits, current 3D ultrasound systems do not provide the real-time response clinicians are accustomed to with conventional 2D ultrasound. The main stages of 3D ultrasound are classified into acquisition,

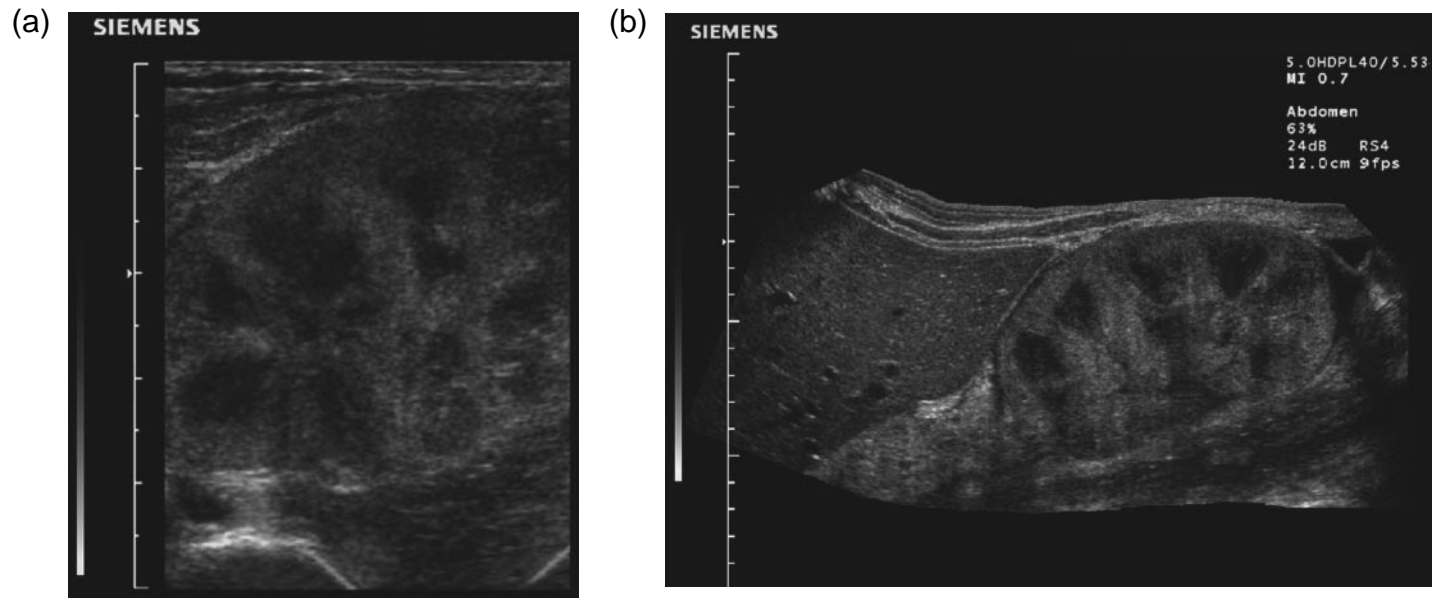


**FIGURE 9** (a) Standard field of view of a renal transplant. (b) Panoramic image displaying the renal transplant, liver, and distal fluid collection. (Images provided by Siemens Medical Systems of Issaquah, WA.)

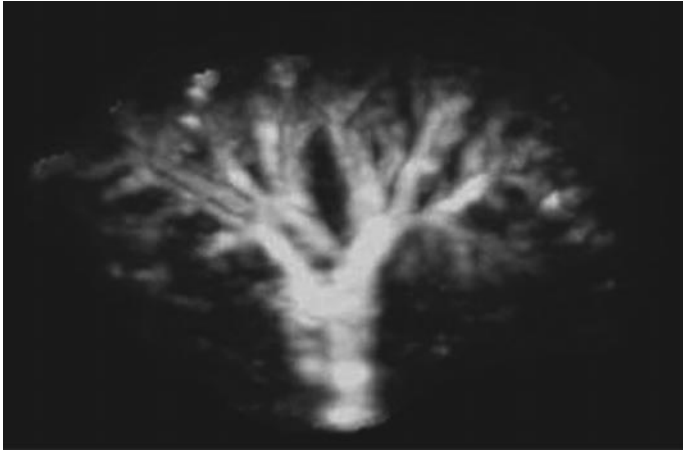


**FIGURE 10** The 3D rendered kidney using maximum intensity projection used for vasculature visualization and volume estimation.

reconstruction, and visualization, each posing a challenge to real-time processing and feedback.

### Acquisition

Volumes are typically generated by first obtaining a sequence of spatially registered 2D images. To spatially register the 2D images, a method must be used to determine the position and orientation of the acquired 2D images relative to a common spatial coordinate system. The two main approaches today include mechanical versus freehand scanning, with 2D array transducers a possibility in the future (106).

With mechanical scanning, the transducer is mounted in a mechanical device, which then moves the transducer in a precise manner about one dimension. The movement can be classified as linear, fan, and rotational (35). With linear scanning, parallel and equidistant 2D images are acquired, creating a cube that can be efficiently reconstructed as the data naturally align with memory storage. With fan scanning, 2D images are acquired in an arc by rotating the transducer about its face in the elevation direction (28), which allows for a small assembly and single contact point useful in confined spaces, like transesophageal imaging (61). Similarly, rotational scanning, in which the transducer is rotated about its central axis, has found use in transesophageal (88) and transthoracic 3D imaging (59). Mechanical systems are inexpensive, provide very accurate localization, and facilitate reconstruction owing to their predefined geometry. However, they tend to be bulky and difficult to use over the irregular surfaces of the body.

Freehand systems allow fairly unconstrained movement of the transducer over the patient, similar to 2D ultrasound imaging to which the clinicians are accus-

tomed. The only constraint to the clinician is to avoid moving the transducer too quickly during scanning, leaving gaps between 2D images. This can be minimized by providing real-time feedback to the clinician during scanning by displaying the volume incrementally as it is being scanned (74). To register the 2D images with freehand acquisition, a 6 degree-of-freedom (DOF) position and orientation measurement device can be attached to the ultrasound probe, which reports the location of the probe relative to a reference coordinate system. Both acoustical (65, 50) and electromagnetic (29, 33, 74) sensors have been used. These freehand systems are not as accurate as the mechanical systems, and they tend to be sensitive to environmental changes, such as temperature and humidity for acoustical sensors and electromagnetic interference for the electromagnetic sensors. However, researchers have shown that freehand systems with position sensors can be used to measure distances and volumes within the reconstructed data set fairly accurately (78, 86). Sensorless freehand systems have been recently developed, in which registration is performed by correlating homogeneous speckle regions between images, then using these correlation points to estimate the image rotation, translation, and displacement between images (55b). The accuracy of sensorless registration depends on the tissue speckle characteristics being scanned and currently it is not as accurate as other methods.

In the future, 2D phased-array transducers could greatly improve the clinical acceptance of 3D imaging. With a 2D phased array, both the acquisition time and the accuracy could be improved as the transducer movement is replaced by electronically steering and focusing the beam in both elevation and azimuth (106). The acquisition rate could be such that real-time 3D echocardiology becomes a possibility. However, there are still many technical hurdles to overcome, e.g. the manufacturing of a large number of array elements and receivers. In addition, 2D arrays will still have a similar problem that 1D arrays have when trying to image large organs outside their field of view. Developing a 3D extended-field-of-view capability, which would incrementally create a panoramic 3D image as the 2D transducer is swept over a region, is one possible solution (33b).

## Reconstruction Techniques

Once a sequence of 2D ultrasound images and their corresponding position and orientation information have been acquired, images can be reconstructed into a 3D volume. The most common reconstruction process involves distributing the pixel values of the acquired 2D images into a 3D Cartesian volume of voxels, which is an efficient format to later visualize (or render) the 3D data (74). With the position and orientation information, each image is spatially registered, transforming the coordinates of each pixel into a common reference coordinate system of the volume. Given the coordinates relating the input pixels to the output voxels, the pixel distribution is then performed using either a forward-mapping or reverse-mapping technique. In reverse-mapping, each voxel location in the reconstruction volume is inverse transformed and the value for that location is interpolated from

the nearest pixels in the source images (99). Reverse mapping is efficient for the mechanical acquisition systems (i.e. linear, fan, and rotational) that have a pre-determined geometry with a well-defined scanning motion. The unconstrained motion for freehand systems is better suited for forward mapping, in which the input pixels are mapped to locations within the reconstruction grid and their pixel values distributed to the nearest voxels in the volume (74). Simple and fast techniques to distribute the pixels are widely used, such as replacement value, maximum value, and pixel averaging (33). These techniques typically project either the maximum or the average value of the incoming pixel value and previous neighboring voxels values. The resulting value is then distributed to the eight surrounding neighbor voxels, which aids in reducing “gaps” in the volume.

The reconstruction process typically preserves all the original image information in the 3D volume; thus, either the volume or surface rendering visualization techniques can later be used. Another approach is to presegment the acquired 2D images before reconstruction (35). For surface rendering, this can greatly reduce the data size and lead to fast rendering.

## Visualization

The techniques for visualizing the ultrasound volume data can be categorized into multiplanar, volume-based, and surface-based viewing (35). With multiplane viewing, arbitrary 2D image slices are resampled from the volume, appearing as conventional B-mode images clinicians are accustomed to. One approach is to provide the 3D information (or cues) by displaying three perpendicular slices simultaneously (70). Another technique is to map the slices to the surface of a rotating cube (99).

To visualize the surface of organs or structures like arteries, surface rendering is used, shading and illuminating the surfaces such that the 3D object appears to have depth. Before rendering, the objects in the volume must be segmented and classified, using either manual or automatic methods. Segmenting the images manually leads to more precise boundaries, but it takes too long in the routine clinical environment. Thus, automated methods are needed, such as by Chen et al (18) for the prostate and Coppini et al (21) for the left ventricle. Several examples of surface rendering can be found in echocardiography (21) and obstetrics (70).

With volume-based rendering, the information within the entire 3D volume is projected onto a 2D-image plane. Ray casting is normally used, in which rays are projected through the 3D volume and the final value assigned to the projected ray is based on some function of the voxel values along the ray path. A simple function is to assign the ray value to either the maximum voxel value along the ray (maximum intensity projection) or the minimum voxel (minimum intensity projection). The maximum-intensity-projection technique is useful if the object is much brighter than surrounding structures, such as the fetal spine (71), whereas the minimum intensity projection technique is useful if the object of interest is

much darker than the surrounding structures, such as vascular anatomy (35). With volume-based rendering, the organs appear translucent, presenting more information to the clinician about the entire 3D volume than with surface or multi-planar rendering. However, interpreting the object is not as intuitive as the normal 2D images to which we are accustomed; thus, some training is required. Static views of volume-based rendered objects (such as in Figure 10) can be difficult to interpret, as depth information is not preserved. However, if the object can be interactively viewed from different perspectives, the 3D spatial relationships of the objects in the image readily become apparent.

A performance limitation with the ray-casting technique occurs when non-orthogonal projection angles are used, which requires the algorithm to access the data in a nonsequential manner (in a different order than which the data are stored). This access pattern causes heavy input/output penalties and requires many extra calculations to properly resample the volume by using methods such as trilinear interpolation. Lacroute & Levoy (53) developed an efficient ray-casting algorithm called shear-warp factorization, which has a more efficient memory access pattern and requires less computation, while still maintaining image quality by decomposing the rendering transformation into three steps: a 3D shear, a projection of the volume to a 2D intermediate image, and a 2D affine warp.

## Computational Requirements

One of the main limitations of 3D ultrasound systems has been that they have not been able to provide the real-time or interactive feedback, owing to the high computational demands of 3D, resulting in long reconstruction and an excessive time between rendered volumes. Many researchers have evaluated 3D ultrasound systems trying to meet the computational requirements. Ohbuchi et al (74) developed an interactive 3D system with a workstation to digitize sequences of 2D images from a commercial ultrasound machine, a mechanical tracking arm (3 DOF), and a powerful computing platform to reconstruct and render the volume. For an acquired sequence of  $256 \times 256$  images, they reconstructed a  $128 \times 128 \times 128$  volume at 1.7 fps and rendered a small volume ( $65 \times 81 \times 100$ ) by using a special graphics engine (Pixel-Planes 5) at 10 fps. Pretorius & Nelson (84) and Merz et al (63) reported their experiences with a commercial 3D system (Combison 530, Kretztechnik, Austria), which uses a mechanically swept transducer and performs reconstructions in 5 s on average. However, the system requires 2–10 min to generate a cine sequence of surface-rendered views, using a predefined angular viewing range. Von Ramm et al (103) developed a dedicated cardiac 3D scanner with a 2D transducer and special computing hardware to acquire and display volumetric data in real time (22 fps). However, the system is limited to cardiac applications, has low spatial resolution, and is very expensive. A low-cost, high-performance interactive 3D system developed by Edwards et al (33) uses a single programmable mediaprocessor (Texas Instruments TMS320C80) for all the acquisition, reconstruction, and rendering calculations.

This system can perform volume reconstruction for 6 DOF  $512 \times 512$  image sequences at  $>10$  fps and provides interactive rendering with maximum intensity projection at 10 fps for  $128 \times 128 \times 128$  volumes.

## Clinical Applications of 3D

Even with the technical advancements in 3D ultrasound imaging, there has not been a strong clinical justification for 3D imaging by quantitatively demonstrating clinical needs that 3D can address and 2D imaging cannot. Some proposed areas include the estimation of organ volume, surgical planning, and blood-flow computation (35).

Unlike 2D ultrasound imaging that relies on the skill of the clinician and a trial-and-error approach to obtaining good images, 3D imaging has the potential advantage of being more accurate and repeatable between examinations (78). For example, Tong et al (99) and Riccabona et al (86) have demonstrated accurate and repeatable distance and volume estimation for organs, such as the prostate, by using 3D ultrasound imaging. Experiments with 3D imaging for placental volume and fetus size have also shown some promising results (71). The ability to obtain the volume in a single sweep of scans and then display the 2D planes of interest has the potential to reduce the overall examination time since clinicians today can spend much time searching for the ideal scan location and angle.

The use of 3D ultrasound has been suggested in various clinical applications, including vascular imaging, cardiology, obstetrics, gynecology, and urology. Fenster & Downey (35) highlighted several areas that can benefit from 3D ultrasound's ability to show the relationship between known landmarks and structural abnormalities. These areas include the eye (44), fetus (14, 69, 70, 71), kidney (31), gall bladder (38), and breast (66). In vascular imaging, researchers examined 3D views of vessel walls to quantify plaque volume and assess the degree of stenosis, potentially reducing the need for invasive angiography procedures (15). Other researchers created 3D images of blood flow (using color mode) in large vessels, such as the carotid artery or the aorta (83). The 3D power-mode was used in visualizing microvasculature and potentially identifying abnormal vascularity caused by tumors (31). In cardiology, several investigators developed techniques for acquiring 3D images of the heart for purposes of computing chamber volumes and ejection fraction (55, 62). In obstetrics, 3D ultrasound was used to visualize complex anatomical structures and fetal complications, such as facial anomalies (84) and head and spine anomalies (67). In gynecology, researchers used 3D ultrasound to assess the uterus and ovaries and to visualize and compute the volumes of lesions (93). Bonilla-Musoles et al (12) were able to identify an ovarian mass as malignant by using 3D visualization, where 2D ultrasound had identified it as benign. In urology, researchers developed methods for computing the volume of the prostate gland from a series of perpendicular scans from a transrectal probe for the purpose of diagnosis and evaluation of response to treatment (96).

Although most of the above researchers demonstrated their techniques on clinical data and some quantified a physiological condition with 3D imaging, in most of these cases no statistical comparisons to similar 2D ultrasound techniques have been made to determine the relative worth of the 3D techniques. Before 3D ultrasound can gain widespread clinical acceptance like color-flow imaging, further quantitative studies are needed to assess 3D vs 2D imaging, proving that 3D imaging performs significantly better than 2D in clinical situations.

## PROCESSING CHALLENGE

A large amount of computing power is required to support all the processing needs in B-mode imaging, color-flow imaging, and image processing/display. The ultrasound systems are typically implemented in a hardwired fashion by using application specific integrated circuits (ASIC) and electrically programmable logic devices to meet the real-time requirements and reduce the system cost. Basoglu et al (8) estimated these requirements to be  $\sim 31$  BOPS for a system that uses the phase-shift autocorrelation methods for velocity estimation. A system that uses the time-shift cross-correlation methods requires  $\sim 60$  BOPS. To incorporate new features, such as advanced image-processing applications, panoramic imaging, or 3D imaging, will require even more computing power in future machines. These new applications are currently not well defined and are continually evolving. These dynamic applications will require the flexibility to adapt to changing requirements offered by programmable processors, which the hardwired ASIC approach most likely cannot support easily.

The programmable approach is beginning to appear in commercial ultrasound machines, such as recent products by ATL, Siemens, and GE. Siemens integrated an image-processing board with two TMS320C80 mediaprocessors along with the other hardwired boards inside an ultrasound machine (48). The board has clearly demonstrated the advantage of the adaptability of the programmable approach. For example, the mediaprocessors were capable of handling the dynamic processing requirements of panoramic imaging, which requires the registration, warping, and interpolation of multiple images in real time. Since the exact algorithms for panoramic imaging were initially undefined, the ability to modify the programs and iterate the design was crucial to quickly prototype, test, and finalize the application. A hardwired design approach could not have adapted this quickly, and there would have been difficulty creating a working prototype in a reasonable time and cost. This programmable system also has successfully proven the advantage of hardware reuse. The same hardware has been reprogrammed to offer other features in addition to panoramic imaging, such as automatic fetal head measurement (80), fetal abdomen and femur measurement, harmonic imaging, color-flow panoramic imaging, and 3D imaging (33). With next-generation mediaprocessors, computing requirements for a complete ultrasound system could be satisfied by a handful of these processors.

## CONCLUSIONS

In this review, we focused on the various algorithms, processing requirements, and challenges of the core ultrasound modes. B-mode imaging provides 2D gray-scale images of tissue structures in real time and still challenges researchers with the problem of reducing the speckle noise while enhancing the edges, which has been addressed by many nonlinear filters and by temporal, spatial, and frequency compounding. Spectral Doppler and color-flow imaging provide a means of displaying the velocity of blood flow in the vessels and pose researchers several challenges, such as an aliasing limit, the velocity dependence on Doppler angle, the clutter filtering of the vessel wall motion, and a trade-off of the frame rate versus velocity accuracy, spatial resolution, and/or ROI size. To create the final output image requires several image-processing steps, such as scan conversion, frame interpolation, and tissue/flow decision, resulting in a large computation requirement (e.g. 31 BOPS) for modern diagnostic ultrasound machines. Whereas the older, mature modes of B-mode and color flow could be implemented with hardwired components and boards, the newer applications, such as panoramic imaging, 3D imaging, and image feature extraction, are being implemented with programmable processors.

We believe that future ultrasound machines will incorporate programmable processors even more. Not only are faster mediaprocessors emerging on the market, but general-purpose processors are beginning to include mediaprocessor features, such as the Intel Pentium with the MMX extension. While companies probably will not replace all their hardwired ultrasound processing boards with programmable boards in the near future, there are quite a few advantages to a fully programmable system composed of multiple mediaprocessors. The programmable system would require developing only one multiprocessor board, which would be repeated throughout the system, instead of incurring the cost of developing many unique single-function boards as in the current systems. In the current hardwired systems, when a machine is used in B-mode, the color-flow boards sit idle. In a fully-programmable system, the processors can be reused as a machine switches modes. For example, the many processors needed to process color-flow image sequences during scanning can be easily switched to performing 3D rendering during the visualization phase of 3D imaging. Additionally, the programmable system would provide a real-time platform to experiment many new ideas, features, and applications. For example, it may be possible with a fully programmable architecture to radically convert an ultrasound system from using phase-shift (autocorrelation) to time-shift (cross-correlation) velocity estimation without requiring any additional hardware or modifications to the signal processing system. Much of the emphasis would then switch to software development, and new features and applications could be released to the clinicians via software upgrades. With networking capability currently being integrated into ultrasound machines, it would be technically possible in the future for the clinician to download new

applications and software upgrades or completely reconfigure an ultrasound machine through the Internet. The ease of adapting new algorithms to the programmable system should not only encourage the research and development of new applications or better algorithms, but also reduce the time required to bring innovative ideas from the research laboratory into clinical use, providing clinicians with a fast and effective means to enhance the quality of patient care.

Visit the Annual Reviews home page at <http://www.AnnualReviews.org>.

#### LITERATURE CITED

1. Alam SK, Parker KJ. 1995. The butterfly search technique for estimation of blood velocity. *Ultrasound Med. Biol.* 21:657–70
2. Bamber JC. 1986. Adaptive filters for reduction of speckle in ultrasonic pulse echo images. *Ultrasonics* 24:41–44
3. Barber WD, Eberhard JW, Karr SG. 1985. A new time domain technique for velocity measurements using Doppler ultrasound. *IEEE Trans. Biomed. Eng.* 32:213–29
4. Deleted in proof
- 4b. Basoglu C. 1997. A generalized programmable system and efficient algorithms for ultrasound backend processing. Ph.D. Dissertation, Department of Electrical Engineering, University of Washington, Seattle WA
5. Deleted in proof
6. Deleted in proof
7. Deleted in proof
8. Basoglu C, Managuli R, York G, Kim Y. 1998. Computing requirements of modern medical diagnostic ultrasound machines. *Parallel Comput.* 24:1407–31
9. Beach KW. 1992. 1975–2000: A quarter century of ultrasound technology. *Ultrasound Med. Biol.* 18:377–88
10. Berkhoff AP, Huisman HJ, Thijssen JM, Jacobs EMG, Homan RJF. 1994. Fast scan conversion algorithms for displaying ultrasound sector images. *Ultrason. Imaging* 16:87–108
11. Bohs LN, Friemel BH, McDermott BA, Trahey GE. 1993. A real time system for quantifying and displaying two-dimensional velocities using ultrasound. *Ultrasound Med. Biol.* 19:751–61
12. Bonilla-Musoles F, Raga F, Osborne N. 1995. Three-dimensional ultrasound evaluation of ovarian masses. *Gynecol. Oncol.* 59:129–35
13. Bonnefous O, Pesque P. 1986. Time domain-formulation of pulse-Doppler ultrasound and blood velocity estimation by cross correlation. *Ultrason. Imaging* 8:73–85
- 13b. Bonnefous O, Pesque P, Bernard X. 1986. A new velocity estimator for color flow mapping. *IEEE Ultrason. Symp. Proc., Williamsburg*, 2:855–60.
14. Brinkley JF, McCallum WD, Muramatsu SK, Liu DY. 1982. Fetal weight estimation from ultrasonic three-dimensional head and trunk reconstructions: evaluation in vitro. *Am. J. Obstet. Gynecol.* 144:715–21
15. Cavaye DM, Tabbara MR, Kopchok GE, Laas TE, White RA. 1991. Three dimensional vascular ultrasound imaging. *Am. Surg.* 57:751–55
- 15b. Chalana V., Kim Y. 1997. A methodology for evaluation of boundary detection algorithms on medical images. *IEEE Trans. Med. Imaging.* 16:642–52.
16. Chalana V, Linker DT, Haynor DR, Kim Y. 1996. A multiple active contour model for cardiac boundary detection in echocardiographic sequences. *IEEE Trans. Med. Imaging* 15:290–98

17. Chalana V, Winter TC, Cyr DR, Haynor DR, Kim Y. 1996. Automatic fetal size measurements from ultrasound images. *Acad. Radiol.* 3:628–35
18. Chen CH, Lee JY, Yang WH, Chang CM, Sun YN. 1996. Segmentation and reconstruction of prostate from transrectal ultrasound images. *Biomed. Eng. Appl. Basis Commun.* 8.3:287–92
19. Christensen DA. 1996. *Ultrasonic Bioinstrumentation*. New York: Wiley & Sons
20. Deleted in proof
21. Coppini G, Poli R, Valli G. 1995. Recovery of the 3-D shape of the left ventricle from echocardiographic images. *IEEE Trans. Med. Imaging* 14:301–17
22. Deleted in proof
23. Deleted in proof
24. Crass J, Miller C, Cohen AM. 1992. Radiological application of three-dimensional imaging systems. *Semin. Ultrasound CT MR* 13:94–101
25. Deleted in proof
26. Davatzikos C, Bryan RN. 1996. Using a deformable surface model to obtain a shape representation of the cortex. *IEEE Trans. Med. Imaging* 15:785–95
27. DeJong PMG, Arts T, Hoeks APG, Reneman RS. 1990. Determination of tissue motion velocity by correlation interpolation of pulsed ultrasonic echo signals. *Ultrason. Imaging* 12:84–98
28. Delabays A., Pandian NG, Cao QL, Magni G, Schwartz S, et al. 1995. Trans-thoracic real-time three-dimensional echo-cardiography using a fan-like scanning approach for data acquisition. *J. CV Ultrasound Allied Technol.* 12:49–59
29. Detmer PR, Bashein G, Hodges T, Beach KW, Filer EP, Filer EP, et al. 1994. 3D ultrasonic image feature localization based on magnetic scanhead tracking: in vitro calibration and validation. *Ultrasound Med. Biol.* 20:923–36
30. Detmer PR, Bashein G, Martin RW. 1990. Matched filter identification of left-ventricular endocardial borders in transesophageal echocardiograms. *IEEE Trans. Med. Imaging* 9:396–404
31. Downey DB, Fenster A. 1995. Vascular imaging with a three-dimensional power Doppler system. *Am. J. Roentgenol.* 165:665–68
32. Dutt V. 1995. Statistical analysis of ultrasound echo envelope. PhD Diss. The Mayo Grad. Sch., Rochester, MN
33. Edwards WS, Deforge C, Kim Y. 1998. Interactive three-dimensional ultrasound using a programmable multimedia processor. *Int. J. Imaging Syst. Technol.* 9:442–54
- 33b. Edwards WS, Pagonlatos N, Winter T, Shields L, Marsh C, et al. 2000. Three-dimensional ultrasound extended field of view: A method for evaluating large volumes. Submitted to *Ultrasound Med. Biol.*
34. Evans AN, Nixon MS. 1993. Temporal methods for ultrasound speckle reduction. *IEE Texture Anal. Radar Sonar* 1:1–6
35. Fenster A, Downey D. 1996. 3D ultrasound imaging: a review. *IEEE Eng. Med. Biol.* 15.6:41–51
36. Ferrara KW, Algazi VR. 1991. A new wideband spread target maximum likelihood estimator for blood velocity estimation—Part 1: theory. *IEEE Trans. Ultrason. Ferroelectr. Freq. Control* 38:1–16
37. Ferrara KW, DeAngelis G. 1997. Color flow mapping. *Ultrasound Med. Biol.* 23:321–45
38. Fine D, Perring S, Herbetko J, Hacking CN, Fleming JS, et al. 1991. Three-dimensional (3D) ultrasound imaging of the gallbladder and dilated biliary tree: reconstruction from real-time B-scans. *Br. J. Radiol.* 64:1056–57
39. Deleted in proof
40. Hein A, O'Brien WD. 1993. Current time-domain methods for assessing tissue motion by analysis from reflected ultrasound echoes—a review. *IEEE*

- Trans. Ultrason. Ferroelectr. Freq. Control* 40:84–102
41. Hoeks APG, van de Vorst JJW, Dabekausen A. 1991. An efficient algorithm to remove low frequency Doppler signals in digital Doppler systems. *Ultrason. Imaging* 13:135–44
  42. Jensen JA. 1996. *Estimation of Blood Velocities Using Ultrasound*. Cambridge, UK: Cambridge Univ. Press
  43. Deleted in Proof.
  44. Jensen PK. 1992. Ultrasonographic three-dimensional scanning for determination of intraocular tumour volume. *Acta Ophthalmol.* 204:23–25
  45. Kadi AP, Loupas T. 1995. On the performance of regression and step initialized IIR clutter filters for color Doppler systems in diagnostical medical ultrasound. *IEEE Trans. Ultrason. Ferroelectr. Freq. Control* 42:927–37
  46. Kalivas DS, Sawchuck AA. 1990. Motion compensated enhancement of noisy image sequences. *Int. Conf. Acoustics, Speech, Signal Processing, Albuquerque*, 4:2121–24. New York: IEEE
  47. Kasai C, Namekawa K, Koyano A, Omoto R. 1985. Real-time two-dimensional blood flow imaging using an autocorrelation technique. *IEEE Trans. Sonics Ultrason.* 32:458–64
  48. Kim Y, Kim JH, Basoglu C, Winter TC. 1997. Programmable ultrasound imaging using multimedia technologies: a next-generation ultrasound machine. *IEEE Trans. Inf. Technol. Biomed.* 1:19–29
  49. Kimme-Smith C, Tessler FN, Grant EG, Perella RR. 1989. Processing algorithms for color flow Doppler. *IEEE Ultrason.* 2:877–79
  50. King DL, King DLJ, Shao M. 1990. Three-dimensional spatial registration and interactive display of position and orientation of real-time ultrasound images. *J. Ultrasound Med.* 9:525–32
  51. Kremkau FW, Taylor KJW. 1986. Artifacts in ultrasound imaging. *J. Ultrasound Med.* 5:227–37
  52. Kroger K, Massalha K, Dobonici G, Rudofsky G. 1998. Siescape™: a new sonographic dimension with fictive images. *Ultrasound Med. Biol.* 24:1125–29
  53. Lacroute PG, Levoy M. 1994. Fast volume rendering using a shear-warp factorization of the view transformation. *Computer Graphics Proceedings. Annual Conference Series 1994. SIGGRAPH 94 Conference Proceedings, Orlando, FL, ACM.* 24–29 July 1994. *SIGGRAPH Proc.* 451–58
  54. Deleted in proof
  55. Levine RA, Weyman AE, Handschumacher MD. 1992. Three-dimensional echocardiography: techniques and applications. *Am. J. Cardiol.* 69:121–34
  - 55b. Li M. 1996. *U.S. Patent No. 5582173*
  56. Deleted in proof
  57. Lockwood GR, Turnbull DH, Christopher DA, Foster FS. 1996. Beyond 30 MHz: Applications of high-frequency ultrasound imaging. *IEEE Eng. Med. Biol.* 15.6:60–71
  58. Loupas T, McDicken WN, Anderson T, Allan PL. 1994. Development of an advanced digital image processor for real-time speckle suppression in routine ultrasonic scanning. *Ultrasound Med. Biol.* 20:239–49
  59. Ludomirsky A, Silberbach M, Kenny A, Shiota T, Rice MJ. 1994. Superiority of rotational scan reconstruction strategies for transthoracic 3-dimensional real-time echocardiographic studies in pediatric patients with CHD. *J. Am. Coll. Cardiol. Ann. Sci. Sess., Atlanta, A169*. Amsterdam: Elsevier
  60. Magnin PA, Von Ramm OT, Thurstone FL. 1982. Frequency compounding for speckle contrast reduction in phased array images. *Ultrason. Imaging* 4:267–81
  61. Martin RW, Bashein G, Detmer PR, Moritz WE. 1990. Ventricular volume measurement from a multiplanar transeophageal ultrasonic imaging system: an

- in vitro study. *IEEE Trans. Biomed. Eng.* 37:442–49
62. Martin RW, Graham MM, Kao R, Bashain G. 1989. Measurement of left ventricular ejection fraction and volumes with three-dimensional reconstructed transesophageal ultrasound scans: comparison to radionuclide and thermal dilution measurements. *J. Cardiothorac. Anesth.* 3:260–68
  63. Merz E, Bahlmann F, Weber G. 1995. Volume scanning in the evaluation of fetal malformations: a new dimension in prenatal diagnosis. *Ultrasound Obstet. Gynecol.* 5:222–27
  64. Deleted in proof
  65. Moritz WE, Shreve PL, Mace LE. 1976. Analysis of an ultrasonic spatial locating system. *IEEE Trans. Instrum. Meas.* 25:43–50
  66. Moskalik A, Carson PL, Meyer CR, Fowlkes JB, Rubin JM, Roubidoux MA. 1995. Registration of three-dimensional compound ultrasound scans of the breast for refraction and motion correction. *Ultrasound Med. Biol.* 21:769–78
  67. Mueller GM, Weiner CP, Yankowitz J. 1996. Three-dimensional ultrasound in the evaluation of fetal head and spine anomalies. *Obstet. Gynecol.* 88:372–78
  68. Muzzolini R, Yang YH, Pierson R. 1993. Multiresolution texture segmentation with application to diagnostic ultrasound images. *IEEE Trans. Med. Imaging* 12:108–23
  69. Nelson TR, Elvins T. 1993. Visualization of 3D ultrasound data. *IEEE Comput. Graph. Appl.* 13.6:50–57
  70. Nelson TR, Pretorius DH. 1992. Three-dimensional ultrasound of fetal surface features. *Ultrasound Obstet. Gynecol.* 2:166–74
  71. Nelson TR, Pretorius DH. 1995. Visualization of the fetal thoracic skeleton with three-dimensional sonography: a preliminary report. *Am. J. Roentgenol.* 164: 1485–88
  72. Nitzpon HJ, Rajaonah JC, Burckhardt CB, Dousse B, Meister JJ. 1995. A new pulsed wave Doppler ultrasound system to measure blood flow velocities beyond the Nyquist limit. *IEEE Trans. Ultrason. Ferroelectr. Freq. Control* 42:265–79
  73. Novakov EP. 1991. Online median filter for ultrasound signal processing. *Med. Biol. Eng. Comput.* 29:222–24
  74. Ohbuchi R, Chen D, Fuchs H. 1992. Incremental volume reconstruction and rendering for 3D ultrasound imaging. *SPIE Vis. Biomed. Comput.* 1808:312–23
  75. Ophir J, Makland NF. 1979. Digital scan converters in diagnostic ultrasound imaging. *Proc. IEEE* 67:654–64
  76. Deleted in proof
  77. Overbeck JR, Beach KW, Strandness DE. 1992. Vector Doppler: accurate measurement of blood velocity in two dimensions. *Ultrasound Med. Biol.* 18: 19–31
  78. Pagoulatos N, Edwards WS, Haynor DR, Kim Y. 1998. Calibration and validation of free-hand 3D ultrasound systems based on DC magnetic tracking. *SPIE Med. Imaging* 3335:59–71
  79. Parker JA, Troxel DE. 1983. Comparison of interpolating methods for image resampling. *IEEE Trans. Med. Imaging* 2:31–39
  80. Pathak SD, Chalana V, Kim Y. 1996. Interactive automatic fetal head measurements from ultrasound images using multimedia computer technology. *Ultrasound Med. Biol.* 23:665–73
  81. Pathak SD, Grimm PD, Chalana V, Kim Y. 1998. Pubic arch detection in transrectal ultrasound guided prostate cancer therapy. *IEEE Trans. Med. Imaging* 17: 762–71
  82. Deleted in proof
  83. Picot PA, Rickey DW, Mitchell R, Rankin RN, Fenster A. 1993. Three-dimensional colour Doppler imaging. *Ultrasound Med. Biol.* 19:95–104
  84. Pretorius DH, Nelson TR. 1995. Fetal face visualization using three-dimen-

- sional ultrasonography. *J. Ultrasound Med.* 14:349–56
85. Ramamurthy BS, Trahey GE. 1991. Potential and limitations of angle independent ultrasonic imaging of blood flow and tissue motion. *Ultrasound Med. Biol.* 13:252–68
86. Riccabona M, Nelson TR, Pretorius D, Davidson T. 1995. Distance and volume measurement using three-dimensional ultrasonography. *J. Ultrasound Med.* 14:881–86
87. Deleted in proof
88. Roelandt TC, Ten Cate FJ, Vletter WB, Taams MA. 1994. Ultrasonic dynamic three-dimensional visualization of the heart with a multiplane transesophageal imaging transducer. *J. Am. Soc. Echocardiogr.* 7:217–29
89. Deleted in proof
90. Routh HF. 1996. Doppler ultrasound. *IEEE Eng. Med. Biol.* 15:6:31–40
91. Shariati MA, Dripps JH, McDicken WN. 1993. Comparison of color flow imaging algorithms. *Phys. Med. Biol.* 38:1589–1600
92. Deleted in proof
93. Steiner H, Staudach A, Spitzer D, Schaffer H. 1994. Three-dimensional ultrasound in obstetrics and gynaecology: technique, possibilities, and limitations. *Hum. Reprod.* 9:1773–78
94. Steinke W, Els T, Hennerici M. 1992. Comparison of flow disturbances in small carotid atheroma using a multi-gate pulsed Doppler system and Doppler colour flow imaging. *Ultrasound Med. Biol.* 18:11–18
95. Deleted in proof
96. Terris MK, Stamey TA. 1991. Determination of prostate volume by transrectal ultrasound. *J. Urol.* 145:984–87
97. Thomas J, Peters R, Jeanty P. 1991. Automatic segmentation of ultrasound images using morphological operators. *IEEE Trans. Med. Imaging* 10:180–86
98. Deleted in proof
99. Tong S, Downey DB, Cardinal HN, Fenster A. 1996. A three-dimensional ultrasound prostate imaging system. *Ultrasound Med. Biol.* 22:735–46
100. Tortoli P. 1989. A tracking FFT processor for pulsed Doppler analysis beyond the Nyquist limit. *IEEE Trans. Biomed. Eng.* 36:232–37
101. Trahey GE, Allison JW. 1987. Speckle reduction achievable by spatial compounding and frequency compounding: experimental results and implications for target detectability. *SPIE Pattern Recognit. Acoust. Imaging* 768:185–92
102. Deleted in proof
103. Von Ramm OT, Smith SW, Pavy HG. 1991. High-speed ultrasound volumetric imaging system. Part 1. Parallel processing and image display. *IEEE Trans. Ultrason. Ferroelectr. Freq. Control* 38:109–15
104. Wells PNT. 1987. The prudent use of diagnostic ultrasound. *Ultrasound Med. Biol.* 13:391–400
105. Weng L, Tirumalia AP, Lowery CM, Nock LF, Gustafson DE, et al. 1997. Ultrasound extended-field-of-view imaging technology. *Radiology* 203:877–80
106. Whittingham TA. 1997. New and future developments in ultrasonic imaging. *Br. J. Radiol.* 70(Suppl.):119–32
107. York G, Basoglu C, Kim Y. 1998. Real-time ultrasound scan conversion algorithm on programmable mediaprocessors. *SPIE Med. Imaging* 3335:252–62

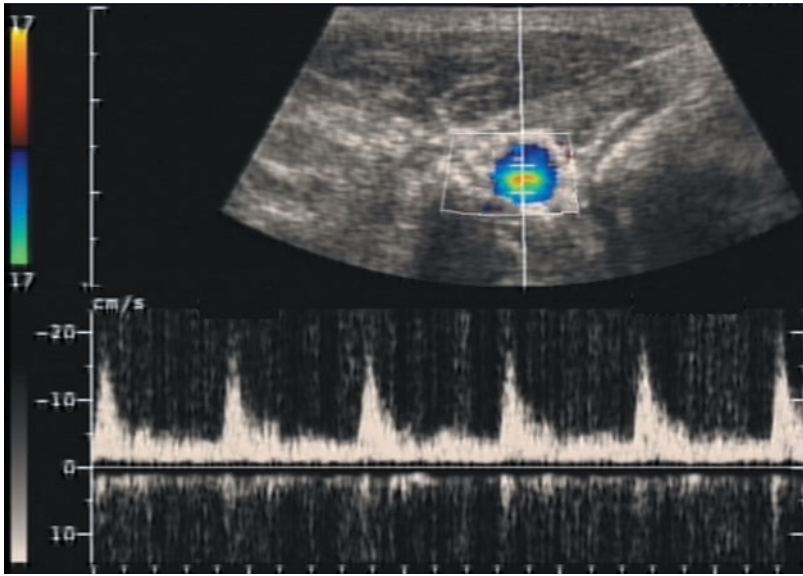


**Figure 2** Example of color-flow image of the carotid artery and the corresponding spectral Doppler spectrogram.



## CONTENTS

A Dedication in Memoriam of Dr. Richard Skalak, <i>Thomas C. Skalak</i>	1
Tissue Engineering: Orthopaedic Applications, <i>C. T. Laurencin, A. M. A. Ambrosio, M. D. Borden, J. A. Cooper Jr.</i>	19
Airway Wall Mechanics, <i>Roger D. Kamm</i>	47
Biomechanics of Microcirculatory Blood Perfusion, <i>Geert W. Schmid-Schönbein</i>	73
Engineering and Material Considerations in Cell Transplantation, <i>Elliot L. Chaikof</i>	103
Bioreactors for Haematopoietic Cell Culture, <i>Lars Keld Nielsen</i>	129
Implanted Electrochemical Glucose Sensors for the Management of Diabetes, <i>Adam Heller</i>	153
Injectable Electronic Identification, Monitoring, and Stimulation Systems, <i>Philip R. Troyk</i>	177
Robotics for Surgical Applications, <i>Robert D. Howe, Yoky Matsuoka</i>	211
Transport of Molecules, Particles, and Cells in Solid Tumors, <i>Rakesh K. Jain</i>	241
Nucleic Acid Biotechnology, <i>Charles M. Roth, Martin L. Yarmush</i>	265
Fluid Mechanics of Vascular Systems, Diseases, and Thrombosis, <i>David M. Wootton, David N. Ku</i>	299
Automatic Implantable Cardioverter-Defibrillators, <i>William M. Smith, Raymond E. Ideker</i>	331
Engineering Aspects of Hyperthermia, <i>Robert B. Roemer</i>	347
3-D Visualization and Biomedical Applications, <i>Richard A. Robb</i>	377
Microfabrication in Biology and Medicine, <i>Joel Voldman, Martha L. Gray, Martin A. Schmidt</i>	401
Engineering Design of Optimal Strategies for Blood Clot Dissolution, <i>Scott L. Diamond</i>	427
Cellular Microtransport Processes: Intercellular, Intracellular and Aggregate Behavior, <i>Johannes M. Nitsche</i>	463
New Strategies for Protein Crystal Growth, <i>J. M. Wiencek</i>	505
Metabolic Engineering, <i>M. Koffas, C. Roberge, K. Lee, G. Stephanopoulos</i>	535
Ultrasound Processing and Computing: Review and Future Directions, <i>George York, Yongmin Kim</i>	559
Telemedicine, <i>Seong K. Mun, Jeanine W. Turner</i>	589
Imaging Transgenic Animals, <i>T. F. Budinger, D. A. Benaron, A. P. Koretsky</i>	611
Instrumentation for the Genome Project, <i>J. M. Jaklevic, H. R. Garner, G. A. Miller</i>	649